GEOCHEMISTRY

Sulfate-dependent reversibility of intracellular reactions explains the opposing isotope effects in the anaerobic oxidation of methane

Gunter Wegener[1,2]*[†], Jonathan Gropp[3]*[†], Heidi Taubner[2,4], Itay Halevy[3], Marcus Elvert[2,4]

The anaerobic oxidation of methane (AOM) is performed by methanotrophic archaea (ANME) in distinct sulfate-methane interfaces of marine sediments. In these interfaces, AOM often appears to deplete methane in the heavy isotopes toward isotopic compositions similar to methanogenesis. Here, we shed light on this effect and its physiological underpinnings using a thermophilic ANME-1–dominated culture. At high sulfate concentrations, residual methane is enriched in both ^{13}C and [2]H ([13]α = 1.016 and [2]α = 1.155), as observed previously. In contrast, at low sulfate concentrations, the residual methane is substantially depleted in [13]C ([13]α = 0.977) and, to a lesser extent, in [2]H. Using a biochemical-isotopic model, we explain the sulfate dependence of the net isotopic fractionation through the thermodynamic drive of the involved intracellular reactions. Our findings relate these isotopic patterns to the physiology and environment of the ANME, thereby explaining a commonly observed isotopic enigma.

INTRODUCTION

The anaerobic oxidation of methane (AOM) with sulfate mitigates the flux of methane (CH_4) from the seafloor into the water column (1, 2). AOM is mediated by anaerobic methanotrophic (ANME) archaea that reverse the methanogenesis pathway to oxidize methane completely to carbon dioxide (CO_2). As ANME archaea cannot reduce sulfate, which is the dominant terminal electron acceptor in marine AOM, they form consortia with sulfate-reducing bacteria (3–5). ANME-1 archaea prevail in deep, diffusion-driven systems not only in anoxic microbial mats but also in hydrothermally heated sediments (6–8). The cultured thermophilic ANME-1 form consortia with the partner bacterium *Candidatus* Desulfofervidus auxilii (9). In these consortia, as well as in other AOM consortia, reducing equivalents are exchanged by direct interspecies electron transfer, which is enabled by a high abundance of cytochromes and pili-based, likely conductive, nanowire networks (5, 10, 11).

The isotopic composition of methane is commonly used to trace its origin and fate in the environment. For carbon and hydrogen, the isotopic compositions, expressed as ratios of the heavy to the light isotope ([13]R = [13]C/^{12}C and [2]R = D/^{1}H, with D = [2]H), are usually reported in δ notation relative to standards (std): $\delta = (^rR_{sample} - {}^rR_{std})/{}^rR_{std} - 1$ [per mil (‰)], where "r" denotes the rare isotope and the standards are Vienna Pee Dee Belemnite (VPDB) for carbon and Vienna Standard Mean Ocean Water (VSMOW) for hydrogen. The isotopic fractionation between a substrate (S) and the product (P) of a reaction is described by

$$^r\alpha_{S/P} = {}^rR_S/{}^rR_P \qquad (1)$$

Close to isotopic equilibrium, methane is depleted in ^{13}C and D relative to CO_2 and H_2O, respectively (12, 13). Farther from equilibrium,

kinetic effects contribute to the net isotopic fractionation, and the usually faster reaction of the substrate molecules containing the light isotopes of carbon and hydrogen results in reaction products that are depleted in the heavy isotopes relative to the substrates. Methanogenesis and methane oxidation under far-from-equilibrium conditions should, therefore, show opposing isotopic effects on methane, respectively depleting and enriching the methane in the heavy isotopes (relative to CO_2 and H_2O). Microbiologically produced methane typically displays strongly negative $\delta^{13}C$ and δD values (14). Moreover, experiments with psychrophilic and mesophilic AOM enrichments incubated at seawater sulfate levels (28 mM) yielded methane that was enriched in ^{13}C and D (relative to CO_2 and H_2O, respectively), with carbon isotope fractionation ([13]α) values between 1.012 and 1.039 and hydrogen isotope fractionation ([2]α) values between 1.109 and 1.315 (15). Evaluations of sediment porewater profiles of methane concentration and isotopic composition yielded similar estimates for [13]α (values between 1.009 and 1.024) during AOM in natural habitats (16–18). A single study from an anoxic water column showed [2]α values consistent with the AOM enrichment experiments (1.120 and 1.157) (19).

Within sediments, AOM concentrates in sulfate methane interfaces (SMIs), where sulfate diffusing from above meets methane rising from below. In these SMIs, methane isotopic compositions often do not match experimental predictions of preferential oxidation of the isotopically light methane isotopomers. Instead, when methane diffusing from below enters the SMIs, its $\delta^{13}C$ values relative to that in the deeper methanogenic zone become frequently lighter by up to 30‰ (20–22). This unexpected observation has been interpreted to reflect either concurrent activity of ANME species and methanogens or that ANME-1 may be facultative methanogens (23–25). However, Yoshinaga and co-workers (22) showed that at low–sulfate concentration AOM cultures can form methane slightly depleted in [13]C. Although concurrent AOM and methanogenesis by the community members in those experiments was not ruled out, the depletion has been alternatively explained by isotopic equilibration between the methane substrate and the dissolved inorganic carbon (DIC) produced through AOM. The authors

[1]Max Planck Institute for Marine Microbiology, 28359 Bremen, Germany. [2]MARUM, Center for Marine Environmental Sciences, University of Bremen, 28359 Bremen, Germany. [3]Department of Earth and Planetary Sciences, Weizmann Institute of Science, Rehovot 7610001, Israel. [4]Faculty of Geosciences, University of Bremen, 28359 Bremen, Germany.
*Corresponding author. Email: gwegener@mpi-bremen.de (G.W.); jonathan.gropp@weizmann.ac.il (J.G.)
†These authors contributed equally to this work.

hypothesized that the gross backward flux from DIC to CH_4 (J_C^-) should be 50 to 75% of the gross forward flux (J_C^+) to generate the observed decrease in $\delta^{13}C$ of methane in SMIs (*22*). This can be recast in terms of a useful concept, the reversibility of the carbon network in AOM, which is defined as the ratio of backward to forward fluxes of AOM (J_C^-/J_C^+). The value of J_C^-/J_C^+ can vary from 0 for an irreversible transformation (i.e., unidirectional oxidation of methane) to 1 for equilibrium between reactant and product (i.e., complete reversibility without net methane oxidation). Within this framework, the results of Yoshinaga and co-workers (*22*) are explained by J_C^-/J_C^+ of 0.50 to 0.75. To reach more pronounced declines of methane $\delta^{13}C$ values in SMIs, J_C^-/J_C^+ would need to increase to even higher values of 0.9 to 0.99 (*26*). However, the AOM reaction is only 2 to 5% reversible at seawater sulfate concentrations (i.e., J_C^-/J_C^+ is only 0.02 to 0.05) (*27, 28*). In addition, radiotracer measurements of the rate of DIC reduction to methane and methane oxidation to DIC rarely yield J_C^-/J_C^+ values greater than 0.2 in marine sediments and microbial mats in which AOM occurs (*29–32*). Last, the Gibbs free energy (ΔG_r) of AOM in most environments is in the range of −20 to −40 kJ mol^{-1} (*33*), more negative than the estimates of the minimal threshold for AOM activity at ~−10 kJ mol^{-1} (*34*), casting further doubt that CH_4 and DIC isotopes nearly equilibrate during AOM in SMIs.

Here, using a thermophilic AOM culture devoid of methanogens, we studied the isotope effects of AOM at different concentrations of its terminal electron acceptor, sulfate. We tracked the isotopic composition and the magnitude of forward and backward fluxes in AOM at an unprecedented level of detail. On this basis, we constructed a multistep biochemical-isotopic model, which resolved shifts in the reversibilities of intracellular reactions as the major cause for the highly variable methane isotope patterns during high-sulfate and low-sulfate AOM.

RESULTS

Methane carbon and hydrogen isotopes during high-sulfate and low-sulfate AOM

To explain the large range of isotopic fractionation observed in AOM, we used an ANME-1–dominated methane-oxidizing enrichment culture (AOM50) obtained from the hydrothermally heated sediment of the Guaymas Basin (*5, 9*). We incubated replicates with initial 11 mM sulfate (high-sulfate experiment) or 1 mM sulfate (low-sulfate experiment) and measured methane carbon and hydrogen isotopic compositions and DIC carbon isotopic compositions during AOM (for all measured values and controls see tables S1 and S2 and data file S1). In both the high-sulfate and low-sulfate experiments, the δD value of H_2O was −54‰ (data file S1).

In the high-sulfate experiment (Fig. 1, A to D), carbon-based rates of net AOM ($J_C^{net} \equiv J_C^+ - J_C^-$) were initially 135 ± 27 µM day^{-1}, but J_C^{net} dropped with declining methane concentrations, as AOM kinetics strongly depend on the availability of methane (*35, 36*). Within this time, the methane $\delta^{13}C$ value increased from −38 to +24‰ (methane $\Delta\delta^{13}C \equiv \delta^{13}C_{final} - \delta^{13}C_{initial} = 62‰$), and the $\delta^{13}C$ value of DIC decreased from −16 to −18‰. On the basis of a Rayleigh distillation model, the value of $^{13}\alpha$ was 1.0158 (±0.001; Fig. 2A). Upon near-complete consumption of methane (after approximately 27 days), J_C^{net} declined to below the detection limit. Reliable methane δD values were limited to the first 20 days of the experiment because of a limit of quantification of 50 µM for hydrogen isotopic analyses [~1000 parts per million (ppm) in the headspace samples]. During this time interval, methane δD values increased from −150‰ to approximately +250‰ (methane $\Delta\delta D \equiv \delta D_{final} - \delta D_{initial} = ~400‰$), and the $^2\alpha$ value was determined to be 1.155 (±0.004; Fig. 2B), relatively low within the range of experimentally determined $^2\alpha$ values for AOM (*15*). These moderate isotope effects during thermophilic AOM are expected at the elevated culture temperatures (*37*).

In the low-sulfate experiment (Fig. 1, E to H) the initial J_C^{net} was substantially lower (83 ± 33 µM day^{-1}), dropping further with increasing sulfate limitation and ceasing altogether when sulfate concentrations were ~50 µM, leaving about 0.5 mM methane that could not be further consumed. Here, methane $\delta^{13}C$ values declined from −38 to −64‰ (i.e., methane $\Delta\delta^{13}C = -26‰$), and $\delta^{13}C$ of DIC remained constant at −16‰. On the basis of a Rayleigh distillation model, the value of $^{13}\alpha$ was 0.977 (±0.006; Fig. 2C). In contrast, methane δD values increased from −150 to about −90‰ in the first 10 days but then dropped to about −120‰ within the next 10 days.
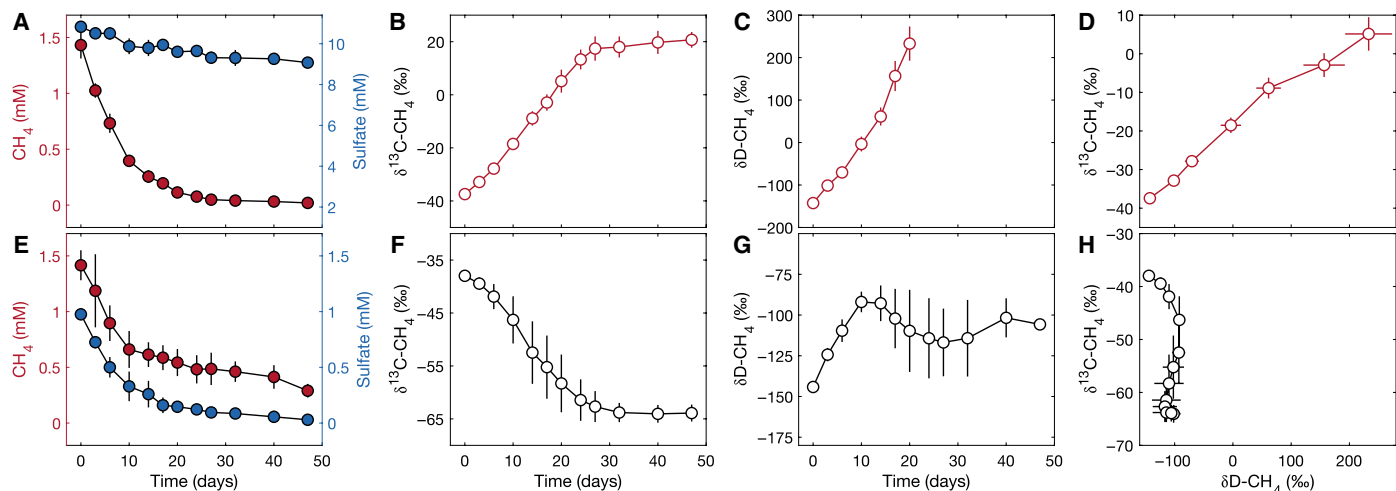

Fig. 1. Temporal evolution of substrate concentrations and isotopic compositions in culture experiments. Incubations were performed with the sediment-free AOM50 culture from the Guaymas Basin. Methane and sulfate concentrations and methane carbon ($\delta^{13}C$) and hydrogen (δD) isotopic compositions in (**A** to **D**) high-sulfate experiments and (**E** to **H**) low-sulfate experiments. Circles represent the mean of four (high-sulfate) and three (low-sulfate) experiments at 50°C. Error bars are the SDs of the measurements (1σ) and are smaller than the symbols where not visible.
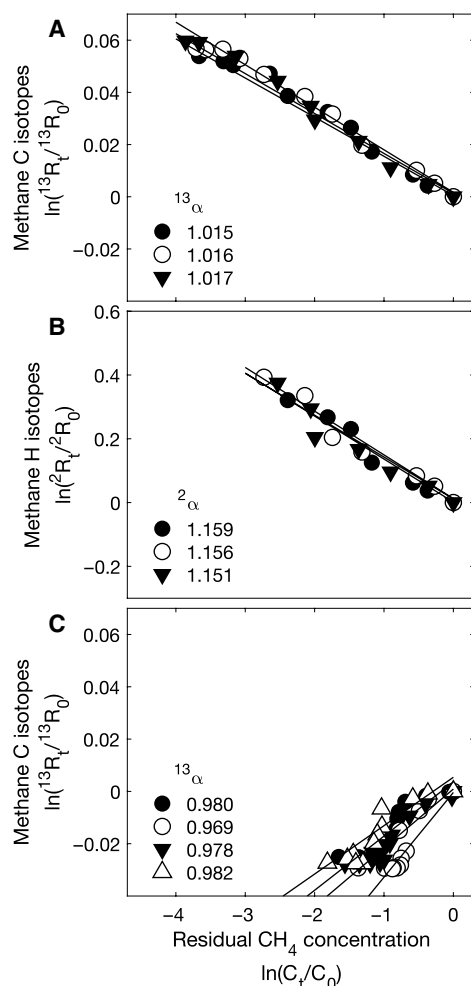
Fig. 2. Determination of carbon and hydrogen fractionation factors for AOM. (**A** and **B**) Calculation of isotopic fractionation factors between CH_4 and CO_2 ($^{13}\alpha$) and CH_4 and H_2O ($^2\alpha$) for high sulfate and (**C**) $^{13}\alpha$ for low sulfate using Rayleigh distillation equations and data from Fig. 1, tables S1 and S2, and data file S1. Data points for the first 25 days (high sulfate) and first 20 days (low sulfate) are included in the calculations, before net methane oxidation was hindered because of substrate limitation.

Notably, both methane $\delta^{13}C$ and δD values stabilized when sulfate was depleted. In a killed control experiment and two abiotic control experiments, the isotopic composition of methane remained relatively stable throughout the experiment ($\Delta\delta^{13}C < 2‰$; $\Delta\delta D < 12‰$; data file S1). Observed minor changes likely result from preferential diffusive loss of isotopically light methane through the stoppers.

Radiotracer-based forward and backward rates of carbon and hydrogen reactions

We resolved the dependence of J_C^-/J_C^+ in the AOM50 culture on sulfate availability by determining J_C^+ and J_C^- in radiotracer assays with ^{14}C-labeled CH_4 and DIC. At sulfate concentrations between 28 and 0.125 mM, J_C^+ gradually declines from ~100 to ~70 μM day^{-1}. J_C^+ dropped to ~40 μM day^{-1} at the lowest sulfate concentrations of 0.05 mM sulfate (Fig. 3A). In contrast, J_C^- initially increased from ~3.5 μM day^{-1} at 28 mM sulfate to 8 μM day^{-1} at 0.25 mM sulfate and decreased to 5.9 μM day^{-1} at 0.05 mM sulfate (Fig. 3B). The

ratio J_C^-/J_C^+ increased from 0.04 at apparently nonlimiting sulfate concentrations (28 and 2.8 mM sulfate) to 0.15 at the lowest sulfate concentrations (0.05 mM sulfate; Fig. 3C). We also inhibited sulfate reduction with 20 mM molybdate. During this treatment, trace rates of J_C^+ and J_C^- of 1.6 ± 0.5 and 0.9 ± 0.2 μM day^{-1} were measured, and the resulting J_C^-/J_C^+ was 0.56.

While CH_4-CO_2 carbon isotope exchange in AOM is limited to a sequential pathway, hydrogen isotope exchange between CH_4 and H_2O occurs in four nonsequential (branched) reactions. Consequently, carbon and hydrogen isotope exchange rates can be decoupled from each other. We assessed the possibility of the differential reversibility of AOM-induced carbon and hydrogen isotope exchange reactions by comparing tritium ($T = {}^3H$) and ^{14}C radiotracer incubations (fig. S1). In incubations with tritium-labeled methane (CH_3T), we measured AOM-induced tritium transfer rates from methane to water (J_H^+, converted to carbon-equivalent rates by dividing by 4) and compared those with rates of J_C^+, as measured in the ^{14}C-CH_4 incubations. While both J_H^+ and J_C^+ declined at sulfate concentrations ≤ 1 mM, J_H^+ declined more gradually, which led to an increase of J_H^+/J_C^+ ratios from 2 to ~8 with decreasing sulfate concentration (fig. S1). We note that the values of J_H^+/J_C^+ reported here are lower limits, as J_H^+ is calculated from the tritium radiolabel experiments under an assumption of no hydrogen isotope fractionation (i.e., the rate of protium transfer from methane to water increases by the same factor as the measured rate of tritium transfer). In the likely event that the transfer is fractionating and that the lighter isotopes of hydrogen react faster than tritium, the values of J_H^+/J_C^+ would be higher.

DISCUSSION

The formation of ^{13}C-depleted methane under net AOM during incubations has been observed before. Incubations of Black Sea AOM-active mats dominated by ANME-1 showed a methane $\Delta\delta^{13}C$ of $-15‰$ at ambient sulfate concentrations of 16 mM, which was explained by a co-occurrence of methanogenesis and AOM (*38*, *39*). Later incubations of cold-adapted AOM cultures dominated by either ANME-1 or ANME-2 resulted in a methane $\Delta\delta^{13}C$ of $-5‰$ at sulfate concentrations below 0.5 mM, which was explained by carbon isotopic equilibration between the reactant CH_4 and the AOM product DIC (*22*). In our experiments, a co-occurrence of AOM and energy-conserving methanogenesis can be excluded, as the AOM50 culture is devoid of gene sequences of known methanogens and methane production could not be stimulated with typical substrates (i.e., dihydrogen, methanol, methylamine, and acetate) (*28*). Hence, all methane isotope effects observed in this culture result from the activity of ANME-1 archaea in association with their partner bacteria. Below, we explore explanations for our experimental results that involve the effects of the evolving ambient conditions on the thermodynamics and kinetics of reactions in the AOM pathway, with implications for other incubation studies and environmental processes.

An influence of sulfate concentration on the reversibility of AOM

We applied the measured concentrations, rates, and J_C^-/J_C^+ values of our experiments to the AOM two-box carbon isotope model of Yoshinaga and co-workers (*22*). For the measured J_C^-/J_C^+ range from 0.04 to 0.15, methane $\delta^{13}C$ and δD values increased under both
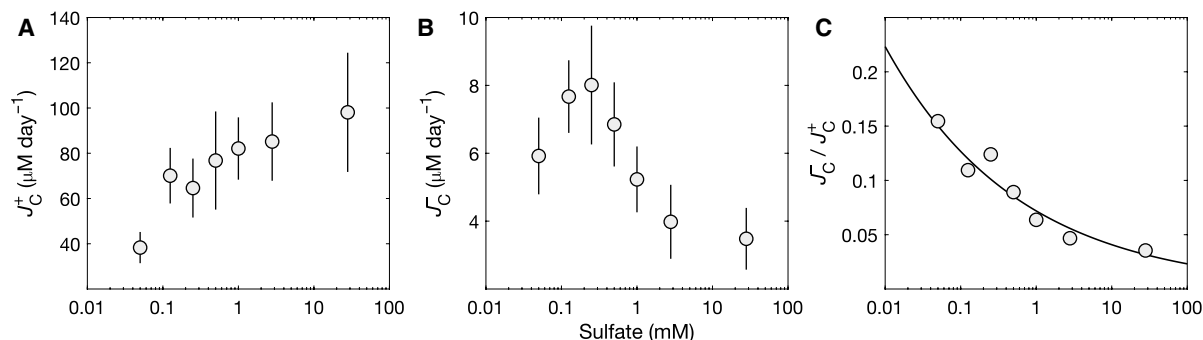
Fig. 3. Forward and backward AOM reaction rates during thermophilic AOM at different sulfate concentrations. (**A**) Determination of AOM forward carbon flux (J_C^+) based on tracer transfer experiments $^{14}CH_4 \rightarrow DI^{14}C$ and (**B**) backward carbon flux (J_C^-) based on $DI^{14}C \rightarrow {}^{14}CH_4$ experiments [$n = 5$ for both (A) and (B); error bars represent 1σ SD]. (**C**) The net reversibility of the AOM reaction as a function of sulfate concentration, presented as the ratio of the backward to forward fluxes (J_C^-/J_C^+, unitless). The line is a fit to the data with the equation $J_C^-/J_C^+ = 0.0719 \times [SO_4^{2-}]^{-0.246}$ ($R^2 = 0.94$).

high-sulfate and low-sulfate conditions because of dominant expression of normal kinetic carbon and hydrogen isotope effects (fig. S2, A and B). This calculated result is inconsistent with the substantial ^{13}C depletion of the residual CH_4 that we observed at the highest reversibilities reached in our experiments, at low sulfate concentration. For such ^{13}C depletion in methane to be reached by the two-box model, J_C^-/J_C^+ would need to be assigned a value of 0.75 (*22*). Consequently, it appears that near-equilibrium carbon isotope exchange between the pathway end-members (CH_4 and CO_2) as an explanation for the decrease in the methane δ^{13}C values during sulfate-limited AOM must be abandoned, especially because this explanation ignores the multistep nature of AOM, in which successive enzymatic steps may exhibit their own reversibilities and isotope effects.

The J_H^+/J_C^+ ratios derived from our radiotracer measurements indicate that carbon-equivalent gross rates of hydrogen transfer from CH_4 to H_2O were, in all cases, higher than the gross rates of carbon transfer from CH_4 to CO_2 (fig. S1). Moreover, the observed increase in J_H^+/J_C^+ from ~2 to ~8 with decreasing sulfate concentration indicates even faster relative rates of gross hydrogen transfer, relative to gross carbon transfer at low sulfate concentrations. We reiterate that actual J_H^+/J_C^+ ratios in our experiments were likely higher than the reported values, as the transfer of protium and deuterium from methane to water is likely faster than the transfer of tritium. Marlow and co-workers (*40*) used a similar approach to constrain AOM rates, by measuring D exchange between mono-deuterated methane (CH_3D) and H_2O. They similarly found that the CH_3D-based AOM rates were higher than the ^{14}C-CH_4 rates by up to a factor of 2, whereas aerobic methanotrophic bacteria did not show such an effect. We suggest that the limited sulfate availability lowers the capacity of the partner bacteria to perform sulfate reduction and to accept reducing equivalents released during AOM. The resulting shortage of electron sinks affects both the thermodynamic drive and the reversibility of AOM, and the kinetics of reactions that depend on the concentrations of the intracellular metabolites whose cycling depends on the existence of electron sinks.

While the net rate of AOM is strongly affected by low sulfate, the stability of the gross forward hydrogen transfer rate (J_H^+) indicates that parts of the pathway are less affected by the shortage of electron sinks. We do not have direct estimates of the reversibility of CH_4-H_2O hydrogen isotope exchange, as J_H^- was not measured. However, since the net carbon and hydrogen reaction rates are linked by the stoichiometry of AOM, stability of J_H^+ coupled to a decrease in the

gross forward carbon transfer rate (J_C^+) suggests increasing reversibility of CH_4-H_2O hydrogen isotope exchange with decreasing substrate concentrations. As our estimates of J_H^+ are lower limits, the increase in the reversibility of CH_4-H_2O hydrogen isotope exchange is likely even more pronounced. We hypothesize that this differential reversibility of individual reactions along the metabolic pathway is the driver of the opposing carbon and hydrogen isotope effects that we observed under the different experimental conditions.

Although the overall J_H^+ values determined in the radiotracer experiments do not reveal the specific reactions that sustain hydrogen isotope exchange, the methyl-coenzyme M reductase (Mcr)- and heterodisulfide reductase (Hdr)–catalyzed reactions are natural candidates to explain this observation. As long as methane is nonlimiting, Mcr may still activate methane molecules to methyl-coenzyme M (CH_3-SCoM) and coenzyme B (HS-CoB), even if sulfate is highly limiting. The deuterium from HS-CoB can then be exchanged with H_2O during HS-CoB cycling by Hdr. In ANME-1, both the Mcr- and Hdr-catalyzed reactions are not coupled to generation of an electrochemical potential across the membrane. Thus, Mcr and Hdr should, in principle, continue to catalyze CH_4-H_2O hydrogen isotope exchange, although perhaps at a slower rate.

The rates of AOM and methanogenesis are often measured by ^{14}C tracer experiments similar to those described here [e.g., (*29, 41*)]. Because of the difference between the gross forward rate of AOM (J_C^+), as measured in radiotracer experiments, and the net AOM rate, $J_C^{net} \equiv J_C^+ - J_C^-$, the use of J_C^+ as a proxy for J_C^{net} results in an overestimation of J_C^{net}, the magnitude of which depends on the magnitude of J_C^-. A 4 to 15% difference between gross and net fluxes, as observed in our experiments, may be acceptable in some conditions, as long as it is accounted for. We note that the difference may be larger under closer-to-equilibrium conditions (e.g., lower methane or sulfate concentrations). The relatively high reversibility of the hydrogen isotope exchange reactions in the pathway, discussed above, leads to marked overestimation of net AOM rates by a factor of at least 2 to 4 when using $^2H(D)$- or $^3H(T)$-labeled methane to constrain J_H^+, even under the relatively far-from-equilibrium conditions in our experiments. Hence, these methods are obviously not ideal to track net AOM rates.

The methane δ^{13}C values appear to level out in both the high-sulfate and the low-sulfate experiments (Fig. 1, B and F). In neither case do the methane δ^{13}C values approach the temperature-dependent CH_4-CO_2 carbon isotope equilibrium, in agreement with the low J_C^-/J_C^+ values derived from our ^{14}C measurements (maximal J_C^-/J_C^+

of 0.15 at 50 μM sulfate). Thus, equilibrium carbon isotope exchange is not the cause of the apparent cessation of change in methane $\delta^{13}C$ values. Instead, near-zero net isotope fractionation may arise because of a fortuitous combination of equilibrium and kinetic carbon isotope effects with opposing values that cancel each other out. In this case, methane $\delta^{13}C$ values will remain invariant upon progressive Rayleigh distillation of the methane pool. Alternatively, invariant methane $\delta^{13}C$ values may arise from a decrease in the gross rates of AOM, which are accompanied by an increase in the turnover time of methane. In this case, the change in methane $\delta^{13}C$ values may become immeasurably slow over the time frame of the experiment, irrespective of the net carbon isotope fractionation.

A multistep isotope model for AOM simulates observed isotope effects

To understand the observed isotopic evolution at a more mechanistic level and to test the hypotheses provided above for the differential sulfate dependence of carbon and hydrogen isotope fractionation during AOM, we developed a metabolic-isotopic model. The model accounts for the effect of step-specific reversibility in the AOM pathway on the net fractionation of carbon and hydrogen isotopes (for model architecture and parameterization, see Materials and Methods and text S1). As in previous studies [e.g., (22)], the model is bound by the concentrations and starting isotopic compositions of the end-members methane, DIC, and water (tables S1 and S2). Unlike previous work, our model includes a subset of the intracellular intermediates in AOM, specifically, CH_3-SCoM, HS-CoB, and formyl methanofuran (CHO-MFR) and the reactions between these metabolites (Fig. 4 and Table 1). We consider these pools as critical because reactions upstream and downstream of these compounds have the most positive and negative standard Gibbs free energy (ΔG_r^0) values in the AOM pathway (42). Upstream of CH_3-SCoM, the positive $\Delta G_r^{'0}$ is likely to lead to high reversibility of the Mcr-catalyzed activation of methane (reaction 1 in Fig. 4). Downstream of CHO-MFR, the large negative $\Delta G_r^{'0}$ is expected to allow low reversibility of the CHO-MFR dehydrogenase (Fmd)–catalyzed reaction (reaction 3 in Fig. 4). Between CH_3-SCoM and CHO-MFR is a chain of reactions catalyzed by five enzymes, which are not explicitly included in the model. Instead, these reactions are merged and referred to as composite reaction 2 (Fig. 4).

Model AOM gross and net rates, and the net reversibility of AOM, are constrained by the experimental radiotracer results and imposed rather than calculated, thereby removing a layer of complexity and uncertainty from the model. We do not use the tritium-based forward rates of CH_4-H_2O hydrogen isotope exchange to constrain the model but note that the model independently reproduces the high reversibility of hydrogen isotope exchange inferred above from the J_C^+ and J_H^+ measurements. With the experimental methane- and sulfate-dependent rates of AOM (fig. S3), the available energy is randomly split among the four individual reactions in the AOM pathway (ΔG_r^i) and values are randomly assigned to the six unknown kinetic fractionation factors (KFFs). Conceptually, the allocation of ΔG_r^i values reflects how the ANME distribute the available thermodynamic drive along the metabolic pathway to maximize growth yield and energy conservation, the latter of which may be of greater importance in our experimental conditions, where growth was minimal.

For any (random) allocation of ΔG_r^i values, we use the mismatch between the model results and the isotopic measurements to constrain
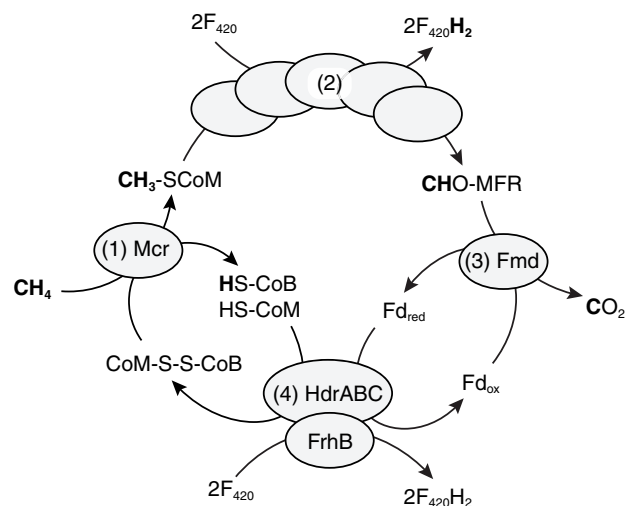

Fig. 4. AOM model architecture. Conceptual model of the ANME partner in the ANME-sulfate reducer consortium in our culture experiments. Each ellipse represents a metabolite pool. In the model, the metabolite pools are related by mass and isotope fluxes of carbon and hydrogen. The carbon and hydrogen atoms that we track in the isotope mass balance are depicted in bold. We assume that the diffusion rate of CO_2, CH_4, and H_2O in and out of the cell is nonlimiting for both the isotope and the mass fluxes. The names of the enzymes that catalyze the reactions included in the model are in the ellipses, numbered as referred to in the text (1 to 4). Note that composite reaction 2 is actually a chain of five reactions in the AOM pathway (see text). The hydrogen in the substrates of reactions 1 and 2 ends up in two distinct products (i.e., CH_4 is oxidized to CH_3-SCoM and HS-CoB, and CH_3-SCoM is further oxidized to CHO-MFR and $F_{420}H_2$).

the parameter values (Fig. 5 and figs. S4 and S5) and the resulting isotopic evolution of CH_4 and DIC (Fig. 6) over the course of an experiment (details in Materials and Methods and text S1). The ultimate model output is a set of best-fit values for the reversibilities (from the ΔG_r^i values) of the four reactions and the six unknown KFFs in the AOM pathway, with an estimate of uncertainty on those values. We note that the modeled isotopic evolution in the different experiments is insensitive to four of the six unknown KFFs (fig. S6). Hence, the model results and inferences drawn from them are robust to the values of these parameters, and in essence, the model may be considered to have six free parameters (four reversibilities and two KFFs).

High-sulfate experiment
During the high-sulfate experiment, the total Gibbs free energy available to the AOM reaction (ΔG_r^{net}) increased from −34 to −19 kJ mol^{-1}, reflecting a weakening of the thermodynamic drive with methane consumption. Over the same time interval, radiocarbon-constrained values of J_C^-/J_C^+ evolved from 0.04 to 0.15, corresponding to a net thermodynamic drive of the carbon pathway in AOM (ΔG_C) in the range −9 to −5 kJ mol^{-1}. The best-fit distribution of this ΔG_C range among the specific pathway steps suggests that the reactions at the beginning and end of the pathway, catalyzed by Mcr and Fmd, respectively (reactions 1 and 3 in Fig. 4), were close to equilibrium (J_1^-/J_1^+ of 0.73 to 0.87 and J_3^-/J_3^+ of 0.63 to 0.83; Fig. 5, A and C). In contrast, the composite reaction 2 was far from equilibrium (J_2^-/J_2^+ of 0.07 to 0.33; Fig. 5B). The hydrogen isotope exchange between HS-CoB and H_2O is catalyzed by the Hdr/coenzyme F_{420} hydrogenase complex (reaction 4 in Fig. 4). This reaction recycles the reduced electron carriers HS-CoB and ferredoxin (Fd), and at the

Table 1. Reactions that are included in the biochemical-isotopic model. The reactions are numbered with respect to Table 1. CoM-SS-CoB, coenzyme M–HTP heterodisulfide; CH_3-SCoM, methyl-coenzyme M; HS-CoB, methyl-coenzyme B; HS-CoM, coenzyme M; F_{420}, oxidized coenzyme F_{420}; $F_{420}H_2$, reduced coenzyme F_{420}; Fd_{ox}, oxidized ferredoxin; Fd_{red}^{2-}, reduced ferredoxin.

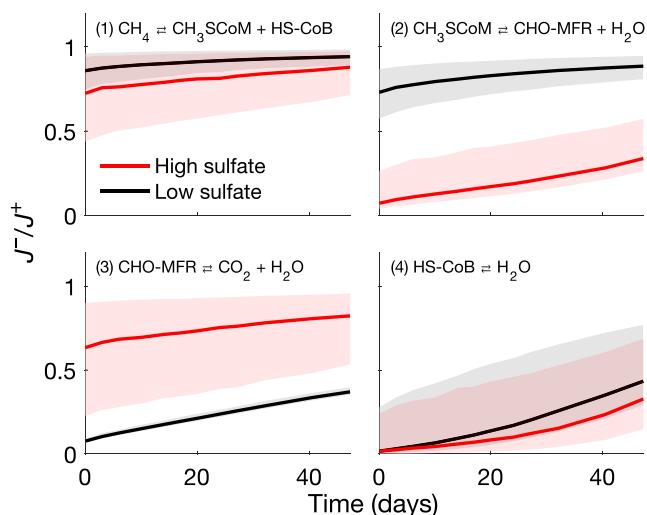|			
1.	$CH_4 + CoM\text{-}SS\text{-}CoB$	$\rightleftharpoons$	$CH_3\text{-}SCoM + HS\text{-}CoB$
2.	$CH_3\text{-}SCoM + 2F_{420} + MFR + H_2O$	$\rightleftharpoons$	$CHO\text{-}MFR + 2F_{420}H_2 + HS\text{-}CoM + H^+$
3.	$CHO\text{-}MFR + Fd_{ox} + H_2O$	$\rightleftharpoons$	$CO_2 + MFR + Fd_{red}^{2-} + 2H^+$
4.	$HS\text{-}CoB + HS\text{-}CoM + Fd_{red}^{2-} + 2F_{420} + 2H^+$	$\rightleftharpoons$	$CoM\text{-}SS\text{-}CoB + Fd_{ox} + 2F_{420}H_2$

Fig. 5. Individual reaction reversibility (J^-/J^+) best fits to the experimental results. The envelopes contain 68% of results based on 10^5 simulations with parameter values drawn from uniform prior distributions and weighted by the inverse of the sum of squared model-measurement mismatch (1/SSE). The schematic chemical reactions in the panels show only the metabolites that participate in isotope exchange, and the full reactions are listed in Fig. 1.

high sulfate concentration, it is out of equilibrium (J_4^-/J_4^+ of 0.01 to 0.32; Fig. 5D). Thus, the increasing methane $\delta^{13}C$ and δD values in the high-sulfate experiments (Fig. 6), which indicate the preferential reaction of isotopically light carbon and hydrogen during AOM to form DIC, reflect a combination of a small equilibrium isotope effect (EIE) between CH_4 and CH_3-SCoM (Mcr-catalyzed reaction) and the partial expression of kinetic isotope effects (KIEs) of composite reaction 2 and the Hdr-catalyzed reactions. The downstream carbon EIE between CHO-MFR and DIC is masked by the irreversibility of composite reaction 2. The net apparent $^{13}\alpha$ value evolves over the course of the high-sulfate simulation from 0.984 to 1.042, and the $^2\alpha$ value evolves from 0.906 to 1.303.

Our suggested mechanism is in agreement with a recent suggestion that the enrichment of the residual methane in the heavy isotopes and the increase in the relative abundance of the "clumped" isotopologue $^{13}CH_3D$ is due to a combination of expression of KIEs and EIEs with a reversibility of the Mcr-catalyzed reaction (J_1^-/J_1^+) up to 0.6 (43). The slightly lower reversibility predicted in that study relative to the range of reversibility that we predict (0.6 versus 0.73 to 0.87) may arise from the different experimental conditions. Experiments in both studies had excess sulfate (>10 mM), but the initial

concentration of methane was much higher in the experiments described by Ono and co-workers (43) than in our experiments (20 mM versus 1.45 mM). Overall, this resulted in continuously higher ΔG_r^{net} and J_C^{net}, which may have driven the Mcr-catalyzed reaction farther from equilibrium (i.e., toward lower reversibility) (42, 43)

Although sulfate was nonlimiting throughout the experiment (>9 mM), we observed a halt in the increase of methane $\delta^{13}C$ values when methane reached ~0.01 mM after ~30 days. The model captures this trend and identifies a small net fractionation of carbon isotopes as the cause. In the beginning of the experiment, composite reaction 2 is out of equilibrium, and the net isotopic fractionation expressed during this reaction is close to its KIE (with a best-fit carbon KIE value of 20‰). As sulfate is used over the course of the experiment, the reversibility of this reaction increases up to 0.33, resulting in combined expression of the KIE and EIE (the EIE is −47‰ at 50°C) (44). After 30 days, the shift from the kinetic end-member toward greater expression of the equilibrium fractionation end-member yields a net carbon isotope fractionation of zero, which translates to a net zero rate of change in methane $\delta^{13}C$ values (Fig. 6A). In the high-sulfate experiment, methane concentrations were too low for δD determinations after 20 days, but the model predicts that methane δD values should continue to increase during the experiment and only plateau after about 40 days (Fig. 6B). With further decline of J_C^{net} and the concurrent increase in J_C^-/J_C^+, we predict that both methane $\delta^{13}C$ and δD values will ultimately decrease toward CH_4-CO_2 and CH_4-H_2O equilibrium values, respectively.

Low-sulfate experiment

In the low-sulfate experiment, ΔG_r^{net} started at −28 kJ mol^{-1} and reached −12 kJ mol^{-1} at the end of the experiment, and we calculated ΔG_C ranging from −8 to −2 kJ mol^{-1}, only slightly more positive than in the high-sulfate experiment. The best fits to the measured isotopic compositions were obtained when the Mcr-catalyzed reaction (reaction 1 in Fig. 4) is near equilibrium (J_1^-/J_1^+ of 0.86 to 0.94; Fig. 5A); the composite reaction 2 departs somewhat from equilibrium (J_2^-/J_2^+ of 0.73 to 0.88), and the Fmd- and Hdr-catalyzed reactions (reactions 3 and 4, respectively, in Fig. 4) are far from equilibrium at the beginning of the experiment and closer to equilibrium at the end (J_3^-/J_3^+ increasing from 0.07 to 0.37 and J_4^-/J_4^+ increasing from 0.02 to 0.43 during the experiment; Fig. 5, C and D). The best-fit J_i^-/J_i^+ values show that all reactions become more reversible (i.e., closer to equilibrium) relative to the high-sulfate conditions, as expected at the lower sulfate concentrations, with the exception of the Fmd-catalyzed reaction (reaction 3), which we discuss below.

The model reveals that the large negative $\Delta\delta^{13}C$ observed in the experiments is not due to near-equilibrium carbon isotope fractionation between DIC and methane during AOM, which should not be
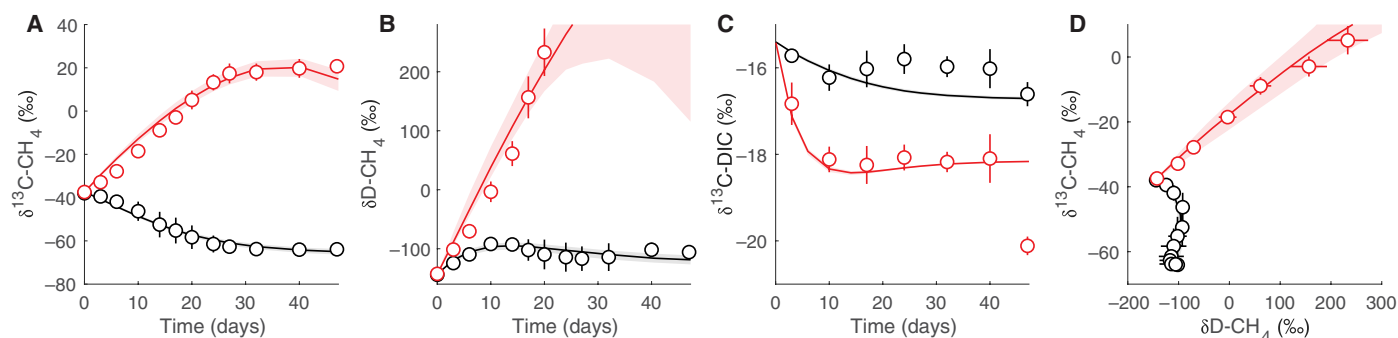
Fig. 6. Modeling of carbon and hydrogen isotopic compositions for high-sulfate and low-sulfate AOM. Temporal evolution of (**A**) methane $\delta^{13}C$ values, (**B**) methane δD values, and (**C**) DIC $\delta^{13}C$ values. (**D**) Comparison of the evolution of methane δD and $\delta^{13}C$ values. Black and red lines are the model results for low-sulfate and high-sulfate conditions, respectively. The circles show the experimental data from Fig. 1. The error bars are the SDs (1σ) and are smaller than the symbols where not visible. The gray and pink envelopes contain 68% of 10^5 model simulations.

expected with the reversibility observed in the low-sulfate experiment ($J_C^-/J_C^+ = 0.15$). The CHO-MFR/CH$_3$-SCoM equilibrium carbon isotope fractionation (composite reaction 2 in Fig. 4) is large and negative (-47‰ at 50°C; (44)), and the net fractionation associated with this reaction is close to this value because of the reaction's high reversibility (J_2^-/J_2^+ of 0.73 to 0.88; Fig. 5B). Together with the negligible EIE of the Mcr-catalyzed reaction (-0.8‰ at 50°C) (44) and the KIE of Fmd (with a best-fit value of ~5‰), net AOM generates methane $\Delta\delta^{13}C$ of up to -26‰, even when J_C^-/J_C^+ is as low as 0.04 to 0.15. The resulting net apparent $^{13}\alpha$ value evolves over the course of the low-sulfate simulation from 0.976 to 0.952. As in the high-sulfate experiment, methane $\delta^{13}C$ stabilizes after ~30 days when 30% of the initial methane still remained (~0.4 mM methane) because of near-complete depletion of the sulfate. At this point, the slow gross rates of AOM, coupled with the relatively large residual pool of methane yield long methane residence times of 70 days after 30 days of experiment and ~400 days at the end of the experiment. The resulting small relative rate of carbon isotope exchange manifests as near-invariant methane $\delta^{13}C$ values at the time scale of the experiment.

Over the same simulated time period, the apparent $^2\alpha$ value evolves from 0.905 to 0.950. The hydrogen isotope exchange network with H$_2$O in AOM is nonlinear and is mediated by the electron carriers HS-CoB and F$_{420}$. In our model, we simplify this system by assuming that F$_{420}$ cycling reactions are at chemical and isotopic equilibrium. In the first days of the low-sulfate experiment, the low J^-/J^+ values of the Fmd-catalyzed reaction (reaction 3 in Fig. 4) result in the expression of hydrogen KIEs and a slight overall increase in methane δD values ($\Delta\delta D > 0$), in contrast to methane $\delta^{13}C$ values, which decrease throughout the experiment (i.e., display $\Delta\delta^{13}C < 0$). As the J^-/J^+ values of the reactions downstream of CH$_3$-SCoM (reactions 2 and 3 in Fig. 4) increase as substrates are consumed and ΔG_C becomes less negative, the EIEs of these reactions are increasingly expressed, pulling methane δD to more negative values and resulting in $\Delta\delta D < 0$. However, methane δD values by the end of the experiment (-115‰) are almost 95‰ heavier than expected at hydrogen isotope equilibrium between CH$_4$ and H$_2$O at the experimental temperature (for the measured H$_2$O δD of -54‰, methane δD at hydrogen isotope equilibrium would be -208‰), suggesting that CH$_4$ remains far from equilibrium with the H$_2$O, even when J_C^{net} is almost zero.

The change in the modeled reversibility of the Fmd-catalyzed reaction between the high-sulfate conditions ($J_3^-/J_3^+ > 0.62$) and low-sulfate conditions (J_3^-/J_3^+ of 0.07 in the beginning, increasing to 0.37) appears counterintuitive. A decrease in sulfate concentrations, through interspecies electron transfer, is expected to decrease the oxidation state of the AOM partner. This may lead to an increase in the ratio of reduced to oxidized electron carriers, which, in turn, leads to a lower thermodynamic drive of the individual reactions in AOM (i.e., an increase in reversibility). However, the adjustment of intracellular metabolite concentrations, other than those of electron carriers, to the lower oxidation state means that while most reactions become less favorable (i.e., more reversible), some may become more favorable (i.e., less reversible). A full metabolic model, which is beyond the scope of the current study, is required to resolve such cases. With the simplified model developed here, we suggest that such a decrease in the reversibility of the Fmd-catalyzed reaction is required to reach agreement between the model and the experimental observations. Such a trend is conserved even when we relax the constraint of consistency between the Gibbs free energy allocated to the different reactions and the J_C^-/J_C^+ determined by radiocarbon measurements (fig. S7).

High-sulfate and low-sulfate AOM experiments reproduce conditions in SMIs

Our stable isotope experimental setups were designed to determine methane carbon and hydrogen isotope effects of AOM under high-sulfate and low-sulfate conditions on laboratory time scales. Nonetheless, these experiments show notable similarity to the conditions that prevail in the environment in terms of concentrations of sulfate, methane, DIC, and sulfide. The main difference is the thermophilic cultivation and the higher methane oxidation rate in the culture [150 µmol (L medium)$^{-1}$ day^{-1}] than those in SMIs [<5 µmol (L sediment)$^{-1}$ day^{-1}]. The higher rates allowed us to perform experiments within a reasonable time but kept energetic conditions that mimic environmental settings. This is in contrast to many similar methanogen culture experiments, which are usually grown at H$_2$ concentrations that are orders of magnitudes higher than those encountered in natural environments and which often are not able to reproduce natural isotope effects [e.g., (45, 46)].

The two contrasting scenarios investigated here reflect conditions in SMIs (1), which often appear only centimeters apart from

each other. The upper section of SMIs bears relatively high sulfate concentrations (>1 mM) and is similar to our high-sulfate experiments. Under these conditions, KIEs prevail as displayed by increasing methane $\delta^{13}C$ and δD values upon progressive methane consumption (Figs. 1B and 6B). Fractionation factors retrieved from our experiments ($^{13}\alpha$ of 1.016 to 1.017 and $^2\alpha$ of 1.151 to 1.159) closely match those inferred from natural studies, where values of $^{13}\alpha$ of 1.002 to 1.024 and $^2\alpha$ of 1.120 to 1.157 have been estimated (16–19).

In the lower section of SMIs, AOM proceeds under very low sulfate concentrations (<<1 mM) and an excess of methane. Here, methane $\delta^{13}C$ values often drop instead of becoming increasingly positive (22, 23, 47). It has been suggested that this decline is caused by high rates of hydrogenotrophic methanogenesis (CO_2 reduction with H_2) that co-occur with active AOM (23, 47, 48). Since ANME-1 archaea are often the only Mcr-containing microorganisms to be found in this part of the SMIs, some have postulated that ANME-1 are facultative methanogens (23, 24, 49). The characterization of ANME-1 as obligate methane oxidizers with no indications of methanogenesis (28) weakens this suggestion. Moreover, for methane $\delta^{13}C$ values to decrease, the apparent rates of CO_2 reduction would need to almost equal AOM rates (22, 38, 48). Radiotracer-based concurrent measurements of methanogenesis and AOM rarely find similar rates of methane production and consumption (24), and in most of these studies, ratios of methane production to consumption in SMIs are lower than 0.2 (29–32). Such low relative ratios of true methanogenesis are unlikely to be responsible for the low methane $\delta^{13}C$ values observed globally in SMIs. Our observations of intrinsic formation of ^{13}C-depleted methane during AOM under substrate limitation resolve this apparent disagreement by obviating the need to invoke methanogenesis by the ANME or other archaea in SMIs. These results notwithstanding, we note that $\delta^{13}C$ values alone are probably insufficient to distinguish between methanogenesis and AOM, in line with previous suggestions about $\delta^{13}C$ values of biomass in sediments from methane seeps and vent sites (50).

As an alternative to concurrent methanogenesis and AOM, Yoshinaga and colleagues (22) suggested that the methane $\delta^{13}C$ decrease may result from carbon isotopic equilibration between methane and DIC, catalyzed by the enzymatic reaction chain of ANME archaea. However, to reach the steep drop in methane $\delta^{13}C$ values observed in deeper zones of SMIs, the reversibility of the net AOM reaction would need to be higher than 0.90 (26, 48). Such high reversibilities contradict the apparent energy yields of AOM under natural conditions of about −20 to −40 kJ mol^{-1}. Instead, our study provides evidence that under conditions of low sulfate availability, intracellular reaction reversibilities along the enzymatic AOM pathway give rise to net fractionations that drive the formation of ^{13}C- and D-depleted methane even with energy yields of −20 kJ mol^{-1} or more. Strongly negative methane $\delta^{13}C$ excursions are specifically found in deep SMIs at sulfate concentrations below approximately 1 mM (21, 22, 26, 51). According to our results, these excursions do not require carbon isotope equilibration between methane and DIC, as proposed by Yoshinaga and co-workers (22). Instead, the $\delta^{13}C$ excursions may be attributed to a combination of EIEs and KIEs associated with relatively high upstream reversibilities (Mcr-catalyzed reaction and the following composite reaction 2) and low downstream reversibility of the final reaction in the AOM pathway, catalyzed by Fmd. In other words, at low sulfate concentrations and on the basis of the experimental results, the multistep model predicts a combination

of high reversibility between the CH_4 substrate and the CHO-MFR intracellular metabolite and an almost irreversible reaction from CHO-MFR to form DIC (Fig. 5). This downstream irreversibility decouples the isotopic composition of methane from variations in the isotopic composition of DIC, which are only partially communicated upstream in the AOM pathway to the methane. Other SMIs, particularly shallow, advection-influenced sites, do not show negative isotope excursions in $\delta^{13}C$ values (52, 53). In these sites, high fluxes of methane into zones of high sulfate availability may prohibit the expression of the above-described effects of low sulfate concentrations on AOM isotope fractionation.

The development of methane δD values within SMIs has been rarely studied (18, 53), but the few available observations are well reproduced by our model. Biogenic methane formed below the SMI is expected to have δD values that reflect CH_4-H_2O near equilibrium. Our experimental and modeling results suggest that in the lower SMI, methane δD values will remain rather constant or will increase slightly, as was observed in our low-sulfate experiment. With increasing sulfate availability in the upper SMI, methane δD values are expected to increase, as the net fractionation is dominated by the normal KIE of composite reaction 2 (i.e., faster reaction of CH_4 with the light hydrogen isotope). The different behavior of methane carbon and hydrogen isotope patterns derives from the effects of a departure from reversibility in a linear versus a branched reaction network. Specifically, high reversibility of the most upstream, Mcr- and Hdr-catalyzed steps of AOM is, in principle, sufficient to result in hydrogen isotope near equilibrium between CH_4 and H_2O but insufficient to result in carbon isotope near equilibrium between CH_4 and DIC.

We further expect a difference in the dependence of methane δD values on those of the water in different parts of the SMI. Under low-sulfate conditions similar to the deeper zone of the SMI, the δD value of the H_2O affects the final methane δD values (fig. S8), as the high reversibility of the Mcr-catalyzed reaction results in partial methane-water hydrogen isotopic equilibration. In high-sulfate conditions that resemble the upper part of the SMI, the δD value of the H_2O has only a small effect on methane δD values (fig. S8), as the lower reversibility of hydrogen isotope exchange reactions results in pronounced expression of KIEs. Under these conditions, Rayleigh distillation of hydrogen isotopes is the main determinant of the methane δD values upon progressive consumption.

We predict that the Mcr-catalyzed reaction will remain close to reversibility for both low-sulfate and high-sulfate conditions, which can explain the trend of equilibration of the clumped isotopologs $^{12}CH_2D_2$ and $^{13}CH_3D$ with time in the environment (54, 55). Ash and co-workers (54), specifically, observed that $\Delta^{12}CH_2D_2$ and $\Delta^{13}CH_3D$ values increase toward the expected temperature-dependent equilibrium value in the deep zone of SMI in brackish sediments from the Baltic Sea. These findings support a pronounced reversibility of parts of the AOM pathway, and our findings identify reversibility in the Mcr-catalyzed reaction as a likely candidate to explain the apparent hydrogen and clumped carbon isotope equilibration in the lower parts of SMIs.

Our combination of AOM culture experiments and biochemical-isotopic modeling suggest that complete CH_4-DIC equilibration is not required for depletion in ^{13}C and D of methane in SMIs. Theoretically, one cannot rule out the possibility that J_C^-/J_C^+ can increase to values higher than 0.15 in natural environments where sulfate concentrations are even lower than in our tracer experiments

(*56*, *57*), and well-adapted wild organisms may still respire, thus potentially driving J_C^-/J_C^+ closer to unity (i.e., full reversibility). However, both the radiotracer rate measurements of gross methane oxidation and DIC reduction and the relatively high ΔG_r^{net} of AOM in most marine environments (−20 to −40 kJ mol^{-1}) support the hypothesis that AOM does not operate close to thermodynamic equilibrium. In the absence of near-equilibrium conditions in the entire AOM pathway, our results provide indications that the expected reversibility landscape of individual pathway steps can explain natural and experimental observations and, specifically, ^{13}C- and D-depleted methane in SMIs at low sulfate concentrations. More broadly, our results highlight the strength of combining carefully tailored culture experiments and metabolic-isotopic models of appropriate complexity to understand the controls on the isotopic compositions of natural biogenic materials.

MATERIALS AND METHODS

Experimental design

This study was conducted to describe the methane carbon and hydrogen isotope effects of AOM in time series and to examine its causes in radiotracer experiments and mass and isotope balance models. For the laboratory experiments, we chose a well-described, sediment-free thermophilic AOM enrichment culture dominated by ANME-1 that is devoid of methanogens. Because of the inherently slow growth of AOM-performing microorganisms, only limited amounts of biomass were available. We chose $n = 3$ or 4 (low and high sulfate, respectively) for the replication of time series experiments and $n = 5$ for radiotracer experiments.

Sample origin and retrieval of thermophilic AOM culture

The thermophilic AOM enrichment derives from hydrothermally heated sediments of the Guaymas Basin, Gulf of California (27°100.437 N, 111°124.548 W), sampled during *RV Atlantis* cruise AT15-56 (submarine ALVIN Dive 4570) in December 2009. Sediment incubations with synthetic marine sulfate reducer medium and methane (0.225 MPa) and further dilution steps at 50°C resulted in sediment-free, highly active AOM biomass (*9*, *58*). The composition and physiological features of this AOM50 culture were described before. The culture was dominated by large consortia of ANME-1 and C*a*. D. auxilii partner bacteria (*9*, *10*, *28*). Other archaea with Mcr-encoding gene sequences have not been detected in this culture. Side community members belong to the Aminicenantes, Chloroflexi, and Lokiarchaea. These organisms may ferment biomass or cell exudates. On the basis of methane-dependent sulfide production rates, the culture shows reproducible doubling times of approximately 50 days. All experiments were performed with the AOM50 culture that was diluted with medium to reach an AOM activity of about 100 to 150 μM day^{-1}. All culture experiments were prepared in a dihydrogen-free, anoxic glove box, and resazurin was added to identify potential contamination with molecular oxygen.

Development of methane $\delta^{13}C$ and δD values during high-sulfate and low-sulfate AOM

The AOM culture (600 ml) was transferred to anoxic medium (*59*) with a reduced sulfate (1 mM) and DIC concentration (10 mM) and evenly distributed into 10 cultivation bottles (256 ml). All samples were filled up with medium, leaving 30-ml headspace and closed with butyl septa. For the high-sulfate experiments, 10 mM MgSO$_4$

(final concentration) was added to three culture replicates: the culture, abiotic controls (only medium) and killed controls (100 mM NaOH final concentration), and additional medium bottles were flushed with 3-atm CH$_4$:CO$_2$ (90:10) and stored for 24 hours on a shaking table (80 rpm) at 50°C. Then, the incubation bottles were completely filled with anoxic seawater medium. The extra medium was connected via Luer Lock tubing (B. Braun, Germany) and needles to the incubation bottles. The incubation bottles were completely filled with medium by gently reducing the pressure.

To measure the CH$_4$ concentration and isotopic composition, preweighed, gas-tight glass vials (12 ml; Exetainer, Labco, UK) with 1 ml of NaOH solution (1 M) and helium atmosphere were prepared. For sulfate and sulfide measurements, 2-ml Eppendorf tubes were filled with 0.5 ml (0.5 M) of zinc acetate solution. Starting after 24 hours, incubations were sampled every 3 to 7 days. Therefore, each culture bottle was sampled through the septum using a syringe, and a headspace was avoided by replacing the sampled volume with sulfate- and methane-free medium. Two milliliters of this sample was injected into the Exetainer vials. The remaining volume was sterile-filtered (0.22-μm membrane filters; Minisart, Sartorius), and 1 ml was mixed into the Zn acetate–containing Eppendorf tubes. To determine DIC concentrations, sterile-filtered medium was filled into headspace-free vials. To measure DIC isotopic compositions, 3.8-ml Exetainer vials were completely filled with sterile-filtered medium. All sampled medium volumes were considered in later calculations.

Preparation of replicate incubations for radiotracer incubations

The sulfate-depleted homogenized AOM50 culture was distributed into Hungate tubes (12 ml in 15-ml incubation tubes). Sulfate or molybdate was added to the different replicate sets ($n = 5$), reaching sulfate concentrations of 28, 2.8, 1, 0.5, 0.25, 0.125, and 0.05 mM and a control with 0 mM sulfate with 10 mM molybdate. A 2.5-atm CH$_4$:CO$_2$ (90:10) atmosphere was supplied to all samples. Samples were equilibrated overnight at 50°C, and vials were completely filled with methane-saturated, sulfate-free medium. Killed controls (one for each sulfate concentration) were prepared with 1-ml NaOH (50%) solution.

Experiments to quantify AOM carbon-based forward (J_C^+) and backward (J_C^-) gross rates

For J_C^+ and J_C^-, the radiotracer ^{14}C-CH$_4$ [6 kilobecquerel (kBq)] or ^{14}C-DIC (30 kBq), respectively, was injected through the stopper and vials were shaken and incubated at 50°C. Replicate samples without tracer were prepared for measurements of DIC and sulfate concentrations and sampled after 24 hours of incubation. The radiotracer incubations were terminated after 48 hours by replacing 9 ml of the medium with 0.5 ml of NaOH (50%) and 8.5 ml of air. The sampled volume was transferred to 20-ml evacuated Hungate tubes with 0.5 ml of NaOH (50%). The excess vacuum was equilibrated with air. To determine J_C^+, the CH$_4$ concentration in both vials was determined by gas chromatography (GC)–flame ionization detection (Thermo Fisher Scientific Focus GC with Supelco Chromosorb 102 column; oven temperature, 40°C; detector temperature, 250°C). For J_C^- measurements, DIC concentrations were determined from replicate vials without tracer addition using the flow injection method (*60*). In both radiotracer experiments, $^{14}CH_4$ and DI^{14}C were separated as described in previous studies (*27*, *61*). The $^{14}CH_4$ activity was determined by

stripping all methane from the vial, its combustion at 850°C with copper oxide catalyst, as described previously, and trapping the methane-derived CO_2 in phenylethylamine. Subsequently, samples were transferred into Erlenmeyer flasks and closed with a rubber stopper. Here, DIC was mobilized with the addition of 5 ml of 6 M HCl, and the produced CO_2 was trapped in a scintillation vial filled with 2 ml of phenylethylamine:NaOH (1 M) 1:1 solution that is hinged into the Erlenmeyer flask ([27]). The samples were mixed with Ultima Gold scintillation cocktail (1:2; Perkin Elmer), and samples were measured by scintillation counting. Contents of radiotracer methane and DIC determined from the two Hungate tubes were combined. The rates of the gross forward AOM rate (J_C^+) were determined from the ^{14}C methane incubation

$$J_C^+ = \frac{DI^{14}C}{^{14}CH_4 + DI^{14}C} \times [CH_4] \times \frac{1}{t} \qquad (2)$$

The gross AOM backward rate (J_C^-) was determined from the ^{14}C tracer contents and the concentrations of DIC and the formed $^{14}CH_4$ in the ^{14}C-$DI^{14}C$ incubations

$$J_C^- = \frac{^{14}CH_4}{DI^{14}C + ^{14}CH_4} \times [DIC] \times \frac{1}{t} \qquad (3)$$

Comparison of the methane-water hydrogen transfer rate, $J_{H'}^+$ and J_C^+ during AOM

AOM50 culture aliquots with different sulfate concentrations were prepared as described above. To determine J_C^+ and J_{H}^+, replicate vials with adjusted sulfate concentrations were treated with $^{14}CH_4$ (~4 kBq) or CH_3T (~883 ± 40 Bq, $n = 7$), respectively, and incubated for 2 days. Additional vials were prepared to confirm the added sulfate concentrations. Samples were incubated for 48 hours, and for J_C^+, samples were treated as described above. To determine J_{H}^+, 1 ml of incubated medium was transferred into 6-ml Exetainer vials with 1 ml of NaOH, and methane concentrations were determined using GC. The additional sample was split into two vials, and tritium-labeled methane CH_3T was removed from the samples by purging with N_2 for 15 min. After that, samples were mixed with scintillation cocktail (Ultima Gold, Perkin Elmer) and measured by scintillation counting. The radioactivity in the added CH_3T was determined from replicate CH_3T samples retrieved at the start of incubations. The tritium transfer rate was calculated according to ([40])

$$J_H^+ = {^3}\alpha \frac{{^3}H\text{-}H_2O}{{^3}H\text{-}CH_4 + {^3}H\text{-}H_2O} \times [CH_4] \times \frac{1}{t} \qquad (4)$$

We assume that tritium transfer can take place in any of the four steps in the metabolic pathway, and not just during methane activation, as was suggested before ([40]). The value of $^3\alpha$ is unknown, and we therefore used a value of 1 for our calculations to produce a lower-limit estimate of J_{H}^+, which we used as a proxy for the total hydrogen transfer rate. A prediction of the tritium kinetic fractionation of the entire pathway would be highly uncertain, but we note that considering a measured $^2\alpha$ of 0.41 for the activation of methane ([62]), and a typical ~1.5 factor for the tritium KIE over the deuterium KIE ([63]), $^3\alpha$ of 0.3 may serve to produce an upper limit estimate for J_{H}^+.

Determination of methane concentrations and carbon and hydrogen isotopic compositions

To determine methane concentrations, 1 ml of the methane Exetainer headspace were injected into the 250-μl gas loop system and analyzed as described above. The detection limit was 5 ppm, equal to 1 μM CH_4 in the medium. Methane carbon isotopic composition was determined using in line combustion to CO_2 using a Thermo Finnigan Trace GC coupled to a Thermo Finnigan Delta plus XP isotope ratio mass spectrometer (IRMS) via a GC-combustion interface III (Supelco Carboxen-1006 PLOT fused-silica capillary column; length, 30 m; internal diameter, 0.32 mm; isothermal column temperature, 40°C).

The stable carbon isotope values of methane are reported in the delta notation ($\delta^{13}C$) relative to the VPDB standard with an analytical precision of 0.28‰, as determined by long-term measurements of an external methane standard of known isotopic composition ($\delta^{13}C = -38.3$‰) relative to an in-house CO_2 reference gas standard. The accuracy obtained for $\delta^{13}C$ values of the methane standard during the analytical campaign was 0.58‰ ($n = 10$). To determine methane hydrogen isotopic composition, the same chromatographic conditions were applied in a GC-IRMS system consisting of a Thermo Fisher Scientific Trace GC IsoLink device, operated in pyrolysis mode producing H_2, coupled via a ConFlow IV interface to a Thermo Fisher Scientific Delta V Plus IRMS. The stable hydrogen isotope values are reported in the delta notation (δD) relative to VSMOW with an analytical precision of 4.8‰, as determined by frequent measurements of an external methane standard of known isotopic composition ($\delta D = -138$‰) relative to an in-house H_2 reference gas standard. The accuracy obtained for δD values of the methane standard during the analytical campaign was 5.5‰ ($n = 29$).

Concentration of DIC

Concentrations of DIC were measured from 1-ml samples retrieved from 0.2-μm filtered medium filled headspace-free into 2-ml glass vials with butyl septum (Zinsser Analytic, Germany). To exclude the effect of sulfide on the measurement, this compound was removed by addition of 100 μl of 0.5 M sodium molybdate solution ([64]). DIC xagainst standards with known concentrations.

Determination of DIC carbon isotopic composition

To determine medium $\delta^{13}C$-DIC values, 100 μl of phosphoric acid (45%) was added to 12-ml Exetainer vials and the headspace was replaced with synthetic air. The filtered medium (1 ml each) was injected using syringe. After 10 hours of equilibration, headspace CO_2 composition was measured by isotope ratio infrared spectroscopy (Thermo Fisher Scientific Delta Ray IRIS with URI connect and Cetac ASX-7100 Autosampler). The $\delta^{13}C$ measurements were calibrated with a reference gas against VPDB and reported with a precision of 0.26‰. The accuracy obtained for $\delta^{13}C$-DIC values during the analytical campaign was 0.17‰ ($n = 9$).

Determination of sulfide and sulfate concentrations

Sulfide and sulfate concentrations were determined from the Zn acetate–fixed medium samples. Exact sample/fixative ratios were determined by weighing empty vials, Zn acetate–filled vials, and vials with samples. To determine sulfide concentrations, zinc acetate–fixed samples were resuspended, and 100-ml aliquots were sampled. Samples were measured using the diamine assay and spectrophotometric detection using standards with known sulfide concentrations ([65], [66]). For sulfate measurements, zinc-fixed samples were 1:50 diluted in

Milli-Q water and measured by ion chromatography (930 compact IC, Metrohm) against standards with known sulfate concentrations.

Determination of net rate and ΔG_r

We calculated the net Gibbs free energy (ΔG_r^{net}) by

$$\Delta G_r^{net} = \Delta G_r^{\prime 0} + RT \ln \frac{\{SO_4^{2-}\}\{CH_4\}}{\{HS^-\}\{HCO_3^-\}} \quad (5)$$

where the curly brackets denote activities. We use activity coefficients of 0.55 for HCO_3^- and HS^-, 0.11 for SO_4^{2-}, and 1 for CH_4 (3) and $\Delta G_r^{\prime 0}$ of −35.8 kJ mol^{-1} at 50°C. We corrected the $\Delta G_r^{\prime 0}$ value for temperature using the integrated Gibbs-Helmholtz equation, resulting in a standard enthalpy change ΔH° of −1 kJ mol^{-1}.

Model for isotope fractionation during AOM

We developed a dynamic isotopic mass balance model to quantify carbon and hydrogen isotope evolution during AOM for the reaction

$$CH_4 + SO_4^{2-} \rightleftarrows HCO_3^- + HS^- + H_2O_{(1)} \quad (6)$$
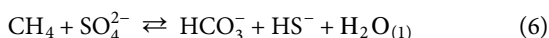
The model is an extension of a previous model for AOM (22), and it simulates the change in the concentration and isotopic composition of methane with time. In this extended model, we divided the sulfate-driven AOM pathway into four subreactions (Fig. 4). Extracellular pools of methane, H_2O, and DIC are assumed to be in chemical and isotopic equilibrium with their intracellular counterparts. We included three additional intracellular pools: CH_3-SCoM, HS-CoB, and CHO-MFR, which are related by mass and isotope fluxes (see model scheme in Fig. 4). The model's tunable parameters are (i) the reversibilities of the four reactions (J_i^-/J_i^+) and (ii) the six unknown KIEs. The overall approach (further described below) was to randomly draw values for these parameters from uniform prior distributions and generate posterior parameter value distributions weighted by the agreement between the model results and the measured isotopic evolution of CH_4 and DIC.

We initiate the model with the initial concentrations of DIC, methane, H_2O, sulfate, and sulfide and the initial carbon and hydrogen isotopic compositions, as measured in the experiments (table S3), and track their change with time by forward integrating the time derivative of each compound. Forward integration is forced with the measured net rate of AOM, based on a linear fit to the residual concentration of methane from the experimental data (fig. S3A), and the net reversibility of the carbon pathway as measured by the ^{14}C tracer experiment (J_C^-/J_C^+). To avoid prior assumptions about the intracellular metabolite concentrations and isotopic compositions, we assume that the cells reach an internal steady state at each time point (see equations S1 to S9 in text S1). As briefly mentioned here, we split the Gibbs free energy available to the ANME among the individual reactions in the pathway (where, by definition, $\sum \Delta G_r^i < \Delta G_r$). The reversibility of the individual reactions, which is defined as the ratio of backward to forward fluxes, J_i^-/J_i^+, can be related to ΔG_r^i through the flux-force theorem (67, 68)

$$J_i^-/J_i^+ = \exp\left(\frac{\Delta G_r^i}{RT}\right) \quad (7)$$

where R is the gas constant and T is the temperature in kelvin. For net AOM, ΔG_r^i values are negative by definition. In sequential metabolic

networks such as for carbon atoms in AOM, J_C^-/J_C^+ is the product of the individual reversibilities in the network (69). This links the reversibility of the reactions between CH_4 and CH_3-SCoM (J_1^-/J_1^+), CH_3-SCoM and CHO-MFR (J_2^-/J_2^+), and CHO-MFR and DIC (J_3^-/J_3^+) to the measured J_C^-/J_C^+ from the ^{14}C tracer incubations through the relation

$$J_C^-/J_C^+ = \exp(\Delta G_C/RT) = \exp(\textstyle\sum_{i=1}^3 \Delta G_r^i/RT) = \\ J_1^-/J_1^+ \times J_2^-/J_2^+ \times J_3^-/J_3^+ \quad (8)$$

where ΔG_C is the time-evolving net thermodynamic drive of the carbon pathway in AOM. We defined ΔG_r^i of reactions 1 to 3 as time-invariant fractions of the total ΔG_C, and in each model time point, we calculated J_i^-/J_i^+ using Eq. 5. The Hdr-catalyzed reaction (reaction 4 in Fig. 4) is not part of the carbon pathway and not bound to J_C^-/J_C^+. We limit ΔG_r^4 so that $\sum_{i=1}^4 \Delta G_r^i$ does not exceed ΔG_r^{net}, taking also into account a minimal threshold of ΔG_r required for sulfate reduction activity of −5 kJ mol^{-1} (50). We note that the model is robust to the choice of a lower threshold for AOM sulfate reduction activity. The fractions of ΔG_r^{net} assigned to the four different reactions were drawn from uniform prior distributions, as described below.

We prescribe the equilibrium isotope fractionation factors between the intermediate metabolites of the AOM pathway (44). We also prescribe the KFFs of the reactions in the AOM pathway, three of which for the Mcr-catalyzed reaction were experimentally determined (table S4) (62) and six of which are unknown and were drawn from uniform prior distributions, as described below.

We randomly drew 10^5 combinations of values from prior uniform distributions of the four fractional ΔG_r^i values and the six unknown KFFs, ran the model with these parameter combinations, and generated posterior distributions of the parameter values weighted by the model-measurement mismatch (the inverse of the sum of squared errors, 1/SSE). The uncertainty envelopes associated with these distributions of model parameters (Fig. 5 and figs. S4 and S5) were used to estimate the uncertainty on the model isotopic evolution (Fig. 6).

Some reactions in the AOM pathway such as the tetrahydromethanopterin S-methyltransferase (Mtr)- and Hdr-catalyzed reactions are involved in cellular energy conservation by coupling potentially endergonic reactions to exergonic reactions. In the Mtr-catalyzed reaction that is included in composite reaction 2, for example, the methyl group transfer from CH_3-SCoM to CH_3-H_4MPT is coupled to transmembrane sodium ion translocation, which, in the case of AOM, is with the chemiosmotic gradient of sodium (70). Accordingly, the reversibility of energy-conserving reactions is determined by a combination of substrate and product activities and by the thermodynamic drive of the process that is coupled to this reaction (71). We do not explicitly model the coupled processes, and the best-fit ΔG_r^i allocation (and associated reversibility) should be considered as implicitly including the effect of their thermodynamic drive on the overall thermodynamic drive of the energy-conserving reactions.

SUPPLEMENTARY MATERIALS

Supplementary material for this article is available at http://advances.sciencemag.org/cgi/content/full/7/19/eabe4939/DC1

View/request a protocol for this paper from Bio-protocol.

REFERENCES AND NOTES

1. N. Iversen, B. B. Jorgensen, Anaerobic methane oxidation rates at the sulfate-methane transition in marine sediments from Kattegat and Skagerrak (Denmark)[1]. *Limnol. Oceanogr.* **30**, 944–955 (1985).

2. W. Reeburgh, Oceanic methane biogeochemistry. *Chem. Rev.* **107**, 486–513 (2007).

3. A. Boetius, K. Ravenschlag, C. J. Schubert, D. Rickert, F. Widdel, A. Gieseke, R. Amann, B. B. Jørgensen, U. Witte, O. Pfannkuche, A marine microbial consortium apparently mediating anaerobic oxidation of methane. *Nature* **407**, 623–626 (2000).

4. V. J. Orphan, C. H. House, K. U. Hinrichs, K. D. McKeegan, E. F. DeLong, Methane-consuming archaea revealed by directly coupled isotopic and phylogenetic analysis. *Science* **293**, 484–487 (2001).

5. G. Wegener, V. Krukenberg, D. Riedel, H. E. Tegetmeyer, A. Boetius, Intercellular wiring enables electron transfer between methanotrophic archaea and bacteria. *Nature* **526**, 587–590 (2015).

6. K. Knittel, A. Boetius, Anaerobic oxidation of methane: Progress with an unknown process. *Annu. Rev. Microbiol.* **63**, 311–334 (2009).

7. W. Michaelis, R. Seifert, K. Nauhaus, T. Treude, V. Thiel, M. Blumenberg, K. Knittel, A. Gieseke, K. Peterknecht, T. Pape, A. Boetius, R. Amann, B. B. Jørgensen, F. Widdel, J. Peckmann, N. V. Pimenov, M. B. Gulin, Microbial reefs in the Black Sea fueled by anaerobic oxidation of methane. *Science* **297**, 1013–1015 (2002).

8. A. Teske, K. U. Hinrichs, V. Edgcomb, A. de Vera Gomez, D. Kysela, S. P. Sylva, M. L. Sogin, H. W. Jannasch, Microbial diversity of hydrothermal sediments in the Guaymas Basin: Evidence for anaerobic methanotrophic communities. *Appl. Environ. Microbiol.* **68**, 1994–2007 (2002).

9. T. Holler, F. Widdel, K. Knittel, R. Amann, M. Y. Kellermann, K. U. Hinrichs, A. Teske, A. Boetius, G. Wegener, Thermophilic anaerobic oxidation of methane by marine microbial consortia. *ISME J.* **5**, 1946–1956 (2011).

10. V. Krukenberg, D. Riedel, H. R. Gruber-Vodicka, P. L. Buttigieg, H. E. Tegetmeyer, A. Boetius, G. Wegener, Gene expression and ultrastructure of meso- and thermophilic methanotrophic consortia. *Environ. Microbiol.* **20**, 1651–1666 (2018).

11. S. E. McGlynn, G. L. Chadwick, C. P. Kempes, V. J. Orphan, Single cell activity reveals direct electron transfer in methanotrophic consortia. *Nature* **526**, 531–535 (2015).

12. Y. Horibe, H. Craig, DH fractionation in the system methane-hydrogen-water. *Geochim. Cosmochim. Acta* **59**, 5209–5217 (1995).

13. J. Horita, Carbon isotope exchange in the system CO_2-CH_4 at elevated temperatures. *Geochim. Cosmochim. Acta* **65**, 1907–1919 (2001).

14. M. J. Whiticar, Carbon and hydrogen isotope systematics of bacterial formation and oxidation of methane. *Chem. Geol.* **161**, 291–314 (1999).

15. T. Holler, G. Wegener, K. Knittel, A. Boetius, B. Brunner, M. M. M. Kuypers, F. Widdel, Substantial 13C/12C and D/H fractionation during anaerobic oxidation of methane by marine consortia enriched in vitro. *Environ. Microbiol. Rep.* **1**, 370–376 (2009).

16. M. J. Whiticar, E. Faber, Methane oxidation in sediment and water column environments—Isotope evidence. *Org. Geochem.* **10**, 759–768 (1986).

17. M. I. Alperin, W. S. Reeburgh, M. J. Whiticar, Carbon and hydrogen isotope fractionation resulting from anaerobic methane oxidation. *Global Biogeochem. Cycles* **2**, 279–288 (1988).

18. C. S. Martens, D. B. Albert, M. Alperin, Stable isotope tracing of anaerobic methane oxidation in the gassy sediments of Eckernförde Bay, German Baltic Sea. *Am. J. Sci.* **299**, 589–610 (1999).

19. W. Reeburgh, S. Tyler, J. Carroll, Stable carbon and hydrogen isotope measurements on Black Sea water-column methane. *Deep-Sea Res. II Top. Stud. Oceanogr.* **53**, 1893–1900 (2006).

20. W. S. Borowski, C. K. Paull, W. Ussler, Carbon cycling within the upper methanogenic zone of continental rise sediments; An example from the methane-rich sediments overlying the Blake Ridge gas hydrate deposits. *Mar. Chem.* **57**, 299–311 (1997).

21. J. W. Pohlman, C. Ruppel, D. R. Hutchinson, R. Downer, R. B. Coffin, Assessing sulfate reduction and methane cycling in a high salinity pore water system in the northern Gulf of Mexico. *Mar. Pet. Geol.* **25**, 942–951 (2008).

22. M. Y. Yoshinaga, T. Holler, T. Goldhammer, G. Wegener, J. W. Pohlman, B. Brunner, M. M. M. Kuypers, K. U. Hinrichs, M. Elvert, Carbon isotope equilibration during sulphate-limited anaerobic oxidation of methane. *Nat. Geosci.* **7**, 190–194 (2014).

23. K. G. Lloyd, M. J. Alperin, A. Teske, Environmental evidence for net methane production and oxidation in putative ANaerobic MEthanotrophic (ANME) archaea. *Environ. Microbiol.* **13**, 2548–2564 (2011).

24. F. Beulig, H. Roy, S. E. McGlynn, B. B. Jorgensen, Cryptic CH_4 cycling in the sulfate-methane transition of marine sediments apparently mediated by ANME-1 archaea. *ISME J.* **13**, 250–262 (2019).

25. R. T. Kevorkian, S. Callahan, R. Winstead, K. G. Lloyd, ANME-1 archaea may drive methane accumulation and removal in estuarine sediments. *Environmental Microbiology Reports* **13**, 185–194 (2020).

26. P. C. Chuang, T. F. Yang, K. Wallmann, R. Matsumoto, C. Y. Hu, H. W. Chen, S. Lin, C. H. Sun, H. C. Li, Y. Wang, A. W. Dale, Carbon isotope exchange during anaerobic oxidation of methane (AOM) in sediments of the northeastern South China Sea. *Geochim. Cosmochim. Acta* **246**, 138–155 (2019).

27. T. Holler, G. Wegener, H. Niemann, C. Deusner, T. G. Ferdelman, A. Boetius, B. Brunner, F. Widdel, Carbon and sulfur back flux during anaerobic microbial oxidation of methane and coupled sulfate reduction. *Proc. Natl. Acad. Sci. U.S.A.* **108**, E1484–E1490 (2011).

28. G. Wegener, V. Krukenberg, S. E. Ruff, M. Y. Kellermann, K. Knittel, Metabolic capabilities of microorganisms involved in and associated with the anaerobic oxidation of methane. *Front. Microbiol.* **7**, 46 (2016).

29. B. Orcutt, A. Boetius, M. Elvert, V. Samarkin, S. B. Joye, Molecular biogeochemistry of sulfate reduction, methanogenesis and the anaerobic oxidation of methane at Gulf of Mexico cold seeps. *Geochim. Cosmochim. Acta* **69**, 4267–4281 (2005).

30. B. Orcutt, V. Samarkin, A. Boetius, S. Joye, On the relationship between methane production and oxidation by anaerobic methanotrophic communities from cold seeps of the Gulf of Mexico. *Environ. Microbiol.* **10**, 1108–1117 (2008).

31. T. Treude, V. Orphan, K. Knittel, A. Gieseke, C. H. House, A. Boetius, Consumption of methane and CO_2 by methanotrophic microbial mats from gas seeps of the anoxic Black Sea. *Appl. Environ. Microbiol.* **73**, 2271–2283 (2007).

32. N. J. Knab, B. A. Cragg, E. R. C. Hornibrook, L. Holmkvist, R. D. Pancost, C. Borowski, R. J. Parkes, B. B. Jørgensen, Regulation of anaerobic methane oxidation in sediments of the Black Sea. *Biogeosciences* **6**, 1505–1518 (2009).

33. D. LaRowe, A. W. Dale, P. Regnier, A thermodynamic analysis of the anaerobic oxidation of methane in marine sediments. *Geobiology* **6**, 436–449 (2008).

34. A. W. Dale, P. Regnier, N. J. Knab, B. B. Jorgensen, P. Van Cappellen, Anaerobic oxidation of methane (AOM) in marine sediments from the Skagerrak (Denmark): II. Reaction-transport modeling. *Geochim. Cosmochim. Acta* **72**, 2880–2894 (2008).

35. K. Nauhaus, A. Boetius, M. Krüger, F. Widdel, In vitro demonstration of anaerobic oxidation of methane coupled to sulphate reduction in sediment from a marine gas hydrate area. *Environ. Microbiol.* **4**, 296–305 (2002).

36. C. Deusner, V. Meyer, T. G. Ferdelman, High-pressure systems for gas-phase free continuous incubation of enriched marine microbial communities performing anaerobic oxidation of methane. *Biotechnol. Bioeng.* **105**, 524–533 (2010).

37. H. J. Spero, J. Bijma, D. W. Lea, B. E. Bemis, Effect of seawater carbonate concentration on foraminiferal carbon and oxygen isotopes. *Nature* **390**, 497–500 (1997).

38. R. Seifert, K. Nauhaus, M. Blumenberg, M. Krüger, W. Michaelis, Methane dynamics in a microbial community of the Black Sea traced by stable carbon isotopes in vitro. *Org. Geochem.* **37**, 1411–1419 (2006).

39. V. A. Vavilin, Estimating changes of isotopic fractionation based on chemical kinetics and microbial dynamics during anaerobic methane oxidation: Apparent zero- and first-order kinetics at high and low initial methane concentrations. *Antonie Van Leeuwenhoek* **103**, 375–383 (2013).

40. J. J. Marlow, J. A. Steele, W. Ziebis, S. Scheller, D. Case, L. M. Reynard, V. J. Orphan, Monodeuterated methane, an isotopic tool to assess biological methane metabolism rates. *mSphere* **2**, e00309-17 (2017).

41. A. J. Zehnder, T. D. Brock, Methane formation and methane oxidation by methanogenic bacteria. *J. Bacteriol.* **137**, 420–432 (1979).

42. R. K. Thauer, Anaerobic oxidation of methane with sulfate: On the reversibility of the reactions that are catalyzed by enzymes also involved in methanogenesis from CO_2. *Curr. Opin. Microbiol.* **14**, 292–299 (2011).

43. S. Ono, J. H. Rhim, D. S. Gruen, H. Taubner, M. Kölling, G. Wegener, Clumped isotopologue fractionation by microbial cultures performing the anaerobic oxidation of methane. *Geochim. Cosmochim. Acta* **293**, 70–85 (2021).

44. J. Gropp, M. A. Iron, I. Halevy, Theoretical estimates of equilibrium carbon and hydrogen isotope effects in microbial methane production and anaerobic oxidation of methane. *Geochim. Cosmochim. Acta* **295**, 237–264 (2021).

45. D. L. Valentine, A. Chidthaisong, A. Rice, W. S. Reeburgh, S. C. Tyler, Carbon and hydrogen isotope fractionation by moderately thermophilic methanogens. *Geochim. Cosmochim. Acta* **68**, 1571–1590 (2004).

46. D. T. Wang, D. S. Gruen, B. S. Lollar, K. U. Hinrichs, L. C. Stewart, J. F. Holden, A. N. Hristov, J. W. Pohlman, P. L. Morrill, M. Konneke, K. B. Delwiche, E. P. Reeves, C. N. Sutcliffe, D. J. Ritter, J. S. Seewald, J. C. McIntosh, H. F. Hemond, M. D. Kubo, D. Cardace, T. M. Hoehler, S. Ono, Nonequilibrium clumped isotope signals in microbial methane. *Science* **348**, 428–431 (2015).

47. W. S. Borowski, T. M. Hoehler, M. J. Alperin, N. M. Rodriguez, C. K. Paull, Significance of anaerobic methane oxidation in methane-rich sediments overlying the Blake Ridge gas hydrates. *NASA Ames Res. Cent.* **164**, 87–99 (2000).

48. P. Meister, B. Liu, A. Khalili, M. E. Böttcher, B. B. Jørgensen, Factors controlling the carbon isotope composition of dissolved inorganic carbon and methane in marine porewater: An evaluation by reaction-transport modelling. *J. Mar. Syst.* **200**, 103227 (2019).

49. R. T. Kevorkian, S. Callahan, R. Winstead, K. G. Lloyd, ANME-1 archaea may drive methane accumulation and removal in estuarine sediments. *Environ. Microbiol. Rep.* **13**, 185–194 (2021).

50. M. J. Alperin, T. M. Hoehler, Anaerobic methane oxidation by archaea/sulfate-reducing bacteria aggregates: 2. Isotopic constraints. *Am. J. Sci.* **309**, 958–984 (2009).

51. F. Schubotz, J. S. Lipp, M. Elvert, K.-U. Hinrichs, Stable carbon isotopic compositions of intact polar lipids reveal complex carbon flow patterns among hydrocarbon degrading microbial communities at the Chapopote asphalt volcano. *Geochim. Cosmochim. Acta* **75**, 4399–4415 (2011).

52. J. F. Biddle, Z. Cardman, H. Mendlovitz, D. B. Albert, K. G. Lloyd, A. Boetius, A. Teske, Anaerobic oxidation of methane at different temperature regimes in Guaymas Basin hydrothermal sediments. *ISME J.* **6**, 1018–1031 (2012).

53. K. Yanagawa, A. Ijiri, A. Breuker, S. Sakai, Y. Miyoshi, S. Kawagucci, T. Noguchi, M. Hirai, A. Schippers, J. I. Ishibashi, Y. Takaki, M. Sunamura, T. Urabe, T. Nunoura, K. Takai, Defining boundaries for the distribution of microbial communities beneath the sediment-buried, hydrothermally active seafloor. *ISME J.* **11**, 529–542 (2017).

54. J. L. Ash, M. Egger, T. Treude, I. Kohl, B. Cragg, R. J. Parkes, C. P. Slomp, B. S. Lollar, E. D. Young, Exchange catalysis during anaerobic methanotrophy revealed by $^{12}CH_2D_2$ and $^{13}CH_3D$ in methane. *Geochem. Perspect. Lett.* **10**, 26–30 (2019).

55. E. D. Young, in *Deep Carbon: Past to Present*, B. N. Orcutt, I. Daniel, R. Dasgupta, Eds. (Cambridge Univ. Press, 2019), pp. 388–414.

56. I. H. Tarpgaard, H. Røy, B. B. Jørgensen, Concurrent low- and high-affinity sulfate reduction kinetics in marine sediment. *Geochim. Cosmochim. Acta* **75**, 2997–3010 (2011).

57. I. H. Tarpgaard, B. B. Jørgensen, K. U. Kjeldsen, H. Røy, The marine sulfate reducer *Desulfobacterium autotrophicum* HRM2 can switch between low and high apparent half-saturation constants for dissimilatory sulfate reduction. *FEMS Microbiol. Ecol.* **93**, fix012 (2017).

58. R. Laso-Pérez, V. Krukenberg, F. Musat, G. Wegener, Establishing anaerobic hydrocarbon-degrading enrichment cultures of microorganisms under strictly anoxic conditions. *Nat. Protoc.* **13**, 1310–1330 (2018).

59. F. Widdel, F. Bak, Gram-negative mesophilic sulfate-reducing bacteria, in *The Prokaryotes*, A. Balows, H. G. Trüper, M. Dworkin, W. Harder, K. H. Schleifer, Eds. (Springer, ed. 2, 1992), vol. 4, pp. 3352–3378.

60. P. J. Hall, R. C. Aller, Rapid, small-volume, flow injection analysis for SCO_2, and NH_4+ in marine and freshwaters. *Limnol. Oceanogr.* **37**, 1113–1119 (1992).

61. T. Treude, A. Boetius, K. Knittel, K. Wallmann, B. B. Jorgensen, Anaerobic oxidation of methane above gas hydrates at Hydrate Ridge, NE Pacific Ocean. *Mar. Ecol. Prog. Ser.* **264**, 1–14 (2003).

62. S. Scheller, M. Goenrich, R. K. Thauer, B. Jaun, Methyl-coenzyme M reductase from methanogenic archaea: Isotope effects on label exchange and ethane formation with the homologous substrate ethyl-coenzyme M. *J. Am. Chem. Soc.* **135**, 14985–14995 (2013).

63. J. Bigeleisen, M. Wolfsberg, Theoretical and experimental aspects of isotope effects in chemical kinetics. *Adv. Chem. Phys.* **1**, 15–76 (1957).

64. R. L. Lustwerk, D. J. Burdige, Elimination of dissolved sulfide interference in the flow injection determination of SCO_2, by addition of molybdate. *Limnol. Oceanogr.* **40**, 1011–1012 (1995).

65. J. D. Cline, Spectrophotometric determination of hydrogen sulfide in natural waters. *Limnol. Oceanogr.* **14**, 454, 458 (1969).

66. F. Aeckersberg, F. Bak, F. Widdel, Anaerobic oxidation of saturated-hydrocarbons to Co_2 by a new type of sulfate-reducing bacterium. *Arch. Microbiol.* **156**, 5–14 (1991).

67. J. Bassham, G. Krause, Free energy changes and metabolic regulation in steady-state photosynthetic carbon reduction. *Biochim. Biophys. Acta Bioenerg.* **189**, 207–221 (1969).

68. D. A. Beard, H. Qian, Relationship between thermodynamic driving force and one-way fluxes in reversible processes. *PLOS ONE* **2**, e144 (2007).

69. W. Wiechert, The thermodynamic meaning of metabolic exchange fluxes. *Biophys. J.* **93**, 2255–2264 (2007).

70. B. Becher, V. Muller, G. Gottschalk, N5-methyl-tetrahydromethanopterin:coenzyme M methyltransferase of Methanosarcina strain Gö1 is an Na(+)-translocating membrane protein. *J. Bacteriol.* **174**, 7656–7660 (1992).

71. Q. Jin, C. M. Bethke, A new rate law describing microbial respiration. *Appl. Environ. Microbiol.* **69**, 2340–2348 (2003).

72. W. Mook, J. Bommerson, W. Staverman, Carbon isotope fractionation between dissolved bicarbonate and gaseous carbon dioxide. *Earth Planet. Sci. Lett.* **22**, 169–176 (1974).

Citation: G. Wegener, J. Gropp, H. Taubner, I. Halevy, M. Elvert, Sulfate-dependent reversibility of intracellular reactions explains the opposing isotope effects in the anaerobic oxidation of methane. *Sci. Adv.* **7**, eabe4939 (2021).

Science Advances

Sulfate-dependent reversibility of intracellular reactions explains the opposing isotope effects in the anaerobic oxidation of methane

Gunter Wegener, Jonathan Gropp, Heidi Taubner, Itay Halevy and Marcus Elvert

ARTICLE TOOLS	http://advances.sciencemag.org/content/7/19/eabe4939
SUPPLEMENTARY MATERIALS	http://advances.sciencemag.org/content/suppl/2021/05/03/7.19.eabe4939.DC1
REFERENCES	This article cites 70 articles, 12 of which you can access for free http://advances.sciencemag.org/content/7/19/eabe4939#BIBL
PERMISSIONS	http://www.sciencemag.org/help/reprints-and-permissions

Use of this article is subject to the Terms of Service